https://doi.org/10.15302/planet.2026.26008

RESEARCH ARTICLE

Optimal laser power beaming network for powering Lunar permanently shadowed regions: a coverage–connectivity–cost trade-off

Mengfan TIAN[1], Liangmin YU[1], Yanglong ZHANG[2], Yiqing WANG[2], Pengzhen GUO (✉)[1], Lifang LI (✉)[2,3], Haibo GAO[4], Zongquan DENG[4]

1 National Key Laboratory of Laser Spatial Information, Harbin Institute of Technology, Harbin 150001, China
2 National Key Laboratory of Aerospace Mechanism, Harbin Institute of Technology, Harbin 150001, China
3 National Key Laboratory of Space Environment and Matter Behaviors, Harbin Institute of Technology, Harbin 150001, China
4 State Key Laboratory of Robotics and System, Harbin Institute of Technology, Harbin 150001, China

© The Author(s) 2026. Published by Higher Education Press. This is an open access article under the CC BY license (http://creativecommons.org/licenses/by/4.0)

Abstract Laser-based power transmission holds promise for wirelessly delivering energy from the illuminated rims of lunar permanently shadowed regions (PSRs), due to its high-power density and long-range directional capabilities. Yet the siting of Laser Power Transmission Stations (LPTS) faces severe constraints from rugged polar terrain and spatiotemporally variable illumination, which may impair the stability of energy provision. The paper presents, for the first time, a terrain- and illumination-aware Multi-Objective Genetic Algorithm (MOGA) for optimizing the deployment of multi-point laser power beaming stations, to maximize effective coverage of PSRs and enhance the stability of power delivery. The deployment problem is formulated as a mixed-integer optimization model that jointly selects an optimal subset of candidate sites (discrete variables) and fine-tunes the positions of Laser Emitter Units (LEUs) within selected sites at meter-level precision (continuous variables). Three conflicting objectives are simultaneously optimized: maximizing effective coverage area, maximizing regional connectivity ratio, and minimizing the number of deployed LPTS units. Leveraging the global search capability of MOGA, the proposed method efficiently explores the complex design space to generate a Pareto-optimal solution set. Validated using real topographic data from the Lunar Orbiter Laser Altimeter (LOLA) over the Shackleton Crater region, the optimized deployment scheme significantly outperforms the baseline configuration: effective coverage increases from 10.76% to 27.55%, while regional connectivity improves from 39.93% to 98.92%. This work presents a feasible technical solution for providing stable wireless laser power to PSRs during the establishment of future lunar bases, offering a novel pathway for the deployment of lunar infrastructure and mission planning in upcoming lunar exploration.

Keywords lunar exploration, laser power transmission, deployment optimization, multi-objective genetic algorithm, coverage, regional connectivity

Received November 6, 2025; accepted January 5, 2026

E-mails: guopengzhen@hit.edu.cn (Pengzhen Guo)
lilifang@hit.edu.cn (Lifang Li)

1 Introduction

Laser Wireless Power Transmission (LWPT) technology enables the transfer of solar energy harvested from continuously illuminated regions into high-energy-density laser beams, which traverse complex terrain to precisely illuminate detectors, rovers, or fixed installations situated within permanently shadowed regions (PSRs), thereby facilitating cross-regional resource allocation and eliminating dependence on cables or limited battery capacity (He et al., 2014; Grandidier et al., 2021; Xu et al., 2024a; Zheng et al., 2024). Owing to its core advantages—including high energy density (>1 kW/m^2), precise beam pointing (μrad-level accuracy), and lightweight system architecture—LWPT has emerged as a viable solution for powering future lunar exploration

missions. As humanity enters the third decade of the 21st century, the Lunar—particularly its south polar region—has once again become the focal point of global deep-space exploration. This renewed interest is primarily driven by the confirmed presence of water ice within PSRs (Nozette et al., 2001; Colaprete et al., 2010; Paige et al., 2010; Siegler et al., 2015; Schorghofer, 2022), a critical resource for *In-Situ* Resource Utilization (ISRU). Such resources can be processed into life-support consumables (water, oxygen) and even rocket propellants, laying the material foundation for sustained scientific outposts and future crewed missions to Mars. Flagship programs such as NASA's Artemis Program and China's Chang'e Project aim to progressively establish lunar bases capable of supporting long-term scientific research and resource exploitation (Creech et al., 2022; Wei et al., 2023; Zhong and Yashar, 2023). The lunar south pole is widely regarded as the optimal site for such infrastructure due to the coexistence of Peaks of Eternal Light (PELs)—regions receiving near-continuous solar illumination (Mazarico et al., 2011; Gläser et al., 2014; Wei et al., 2023) and adjacent PSRs harboring valuable volatiles (Nozette et al., 2001; Colaprete et al., 2010; Paige et al., 2010; Siegler et al., 2015; Schorghofer, 2022; Zhang et al., 2024). However, this unique environment presents unprecedented engineering challenges: PELs are often small, fragmented, and topographically complex, while vast PSRs remain perpetually deprived of direct sunlight, rendering energy delivery among facilities a critical bottleneck (Zuniga et al., 2017). Compared with deploying long-distance cabling or relying on finite battery storage, LWPT offers superior flexibility, extended transmission range, and higher energy density.

To date, relevant LWPT research has focused primarily on component-level optimization and ground-based prototyping: Mukherjee et al. (2013) developed a laser power converter using InGaAsP/InP materials for 1.55 μm wavelengths, achieving 42.3% efficiency at 1 kW/m^2 by optimizing carrier extraction and light absorption. Höhn et al. (2016) modeled the optical and electrical behavior of GaAs converters, providing the first systematic study of temperature's impact (250 K−400 K) on optimal wavelength and efficiency. Landis (2020) discussed the conceptual feasibility of using an 810nm laser and GaAs cells for PSR ice detection. Shi et al. (2016) demonstrated a satellite-to-satellite system using an 808 nm laser, achieving 16.08% efficiency over 50−100 meters. Xu et al. (2024a) designed a LWPT system for a lunar rover, achieving maximum ground-test efficiencies of 11.55% (10 m) and 16.44% (100 m). Other studies proposed enhancing system efficiency by improving light uniformity at the receiver (Xu et al., 2024b) or by optimizing the electro-optical conversion at the transmitter using pulsed currents (Zhou and Jin, 2015; Zhou et al., 2020). In summary, while existing research confirms the fundamental feasibility of LWPT systems, its practical deployment in the lunar polar region faces severe physical and system-level challenges. The complex topography of the lunar poles—including craters, ridges, and impact basins—frequently obstructs Line-of-Sight (LoS) paths essential for laser transmission (Wei et al., 2023). Additionally, the actual output power of LPTS is constrained by the local solar illumination ratio at its deployment site. Moreover, micron- and nanometer-scale lunar dust particles suspended along the transmission path induce absorption and scattering effects, leading to non-negligible beam attenuation and reduced transmission efficiency (Naqbi et al., 2024a, 2024b). Furthermore, at the network level, the deployment of a single station is highly susceptible to environmental impacts, resulting in isolated, disconnected coverage islands that cannot support continuous rover mobility or collaborative regional exploration. Ensuring the topological connectivity of covered areas is therefore vital for the mission's success (Abdollahzadeh and Navimipour, 2016; Priyadarshi and Gupta, 2021; You et al., 2021). Despite these critical issues, no study has yet addressed the critical problem of how to systematically optimize a multi-site Laser Power Transmission Station (LPTS) network in complex lunar terrain to balance coverage, connectivity, and deployment cost.

Therefore, to address the aforementioned challenges, this paper proposes a novel a terrain- and illumination-aware Multi-Objective Genetic Algorithm (MOGA) to construct an efficient and stable LPTS network in the lunar south pole's Shackleton basin. The deployment problem is formulated as a mixed-integer optimization problem (MOP), and the NSGA-II algorithm is employed to simultaneously optimize three conflicting objectives. 1) Maximize effective coverage area, 2) maximize regional connectivity, and 3) minimize the number of deployed LPTS units. The principal innovations of this work are the first application of an MOGA framework to the lunar LWPT deployment problem, the integration of a high-fidelity physical model incorporating Mie scattering, and the adoption of a hybrid integer-continuous optimization formulation that simultaneously optimizes macro-scale site selection and micro-scale meter-level positioning. Simulation results, based on Lunar Orbiter Laser Altimeter (LOLA) topographic data, generate a Pareto-optimal front, from which a representative solution is selected that increases effective coverage from 10.76% to 27.55% and improves regional connectivity from 39.93% to 98.92%. This work provides a systematic optimization framework and theoretical foundation for lunar research base construction and deep-space exploration energy supply.

2 Modeling of the lunar surface laser power transmission system

2.1 System architecture of laser wireless power transmission

2.1.1 The multi-site network concept

As established in the introduction, while component-level LWPT research is mature, a system-level deployment strategy is lacking. The rugged lunar terrain ensures that a single LPTS, even one placed in a high-illumination region, will create only isolated "islands" of power due to frequent LoS obstructions. This fragmented coverage is insufficient for missions requiring continuous rover mobility or robust, wide-area operations.

To address this fundamental gap, the core innovation of this paper is to formulate the deployment problem around a multi-site laser power transmission network. This network-centric model shifts the optimization goal away from maximizing a single point-to-point link. Instead, it focuses on optimizing the collective performance of an integrated system of cooperative assets. This network-based formulation introduces several layers of complexity that the model must address as follow.

1) Combined Coverage: the model cannot just assess one link; it must calculate how power from multiple, spatially distinct Laser Emitter Units (LEUs) combines at every point in the target region.

2) Topological Connectivity: the model must explicitly evaluate the spatial topology of the resulting coverage map. The objective is not merely to maximize the total powered area, but to ensure this area forms a large, contiguous region, which is quantified by the regional connectivity metric.

3) System-Level Trade-offs: this approach inherently creates conflicting objectives. Deploying more stations may increase total coverage but can reduce connectivity if the new stations create isolated hotspots, all while increasing deployment cost.

Therefore, this network concept directly leads to the complex, mixed-integer optimization problem solved in this work. The model must simultaneously determine: 1) the optimal subset of candidate sites to activate (a discrete, combinatorial choice) and 2) the precise meter-level positional offsets for each LEU (a continuous, fine-tuning choice).

To mathematically construct and solve this multi-objective optimization problem, we must first rigorously define the physical and functional architecture of the network's components and the energy flow between them. The following section details this system architecture.

2.1.2 System architecture

The lunar south polar multi-site laser power transmission network system modeled in this study is illustrated in Fig. 1(a). It comprises four primary components. 1) The lunar surface environment, 2) Stationary Support Platforms (SSPs), 3) LEUs, and 4) Target Receiving Units (TRUs). SSPs are deployed within Permanently Illuminated Regions (PIRs)—areas with optimal solar exposure—and serve as primary energy harvesters. They convert incident solar radiation into electrical power via onboard photovoltaic arrays and deliver it to LEUs through dedicated power cables. The LEUs, in turn, convert this electrical input into highly directional laser beams that traverse complex terrain to precisely illuminate TRUs—such as rovers or fixed installations—located within PSRs, thereby enabling remote wireless power delivery.

The detailed energy flow and functional roles of each subsystem are depicted in Fig. 1(b).

1) Lunar Surface Environment: the study region centers on the vicinity of Shackleton Crater near the lunar south pole. High-resolution topographic data from NASA's LOLA is employed to perform accurate LoS occlusion analysis, ensuring terrain-aware deployment optimization.

2) Stationary Support Platform: functioning as the system's energy hub, each SSP integrates a Solar Power Unit for electricity generation. To reflect realistic operational constraints, all LPTS units in this study derive their input power solely from solar energy. Multiple candidate SSP sites are predefined, all situated within high-illumination zones. Each SSP is equipped with a 10-meter mast to elevate its solar panels, thereby maximizing insolation capture. Generated power is conditioned and routed via a Power Management and Distribution (PMAD) subsystem through cabling to its associated LEU.

3) Laser Emitter Unit: the LEU constitutes the core element subject to deployment optimization. Mounted on a mobile platform (e.g., a rover chassis approximately 1 m in height), the LEU receives electrical power from its host SSP and converts it into a collimated laser beam at a specified wavelength (e.g., 1064 nm) via its integrated Laser Subsystem. The beam is then shaped and directed toward the target using a Precision Acquisition and Tracking (PAT) system. Critically, this work assumes that each LEU can be offset from its nominal SSP location, enabling fine positional adjustments to identify locally optimal transmission points.

4) Target Receiving Unit: as the energy recipient, the

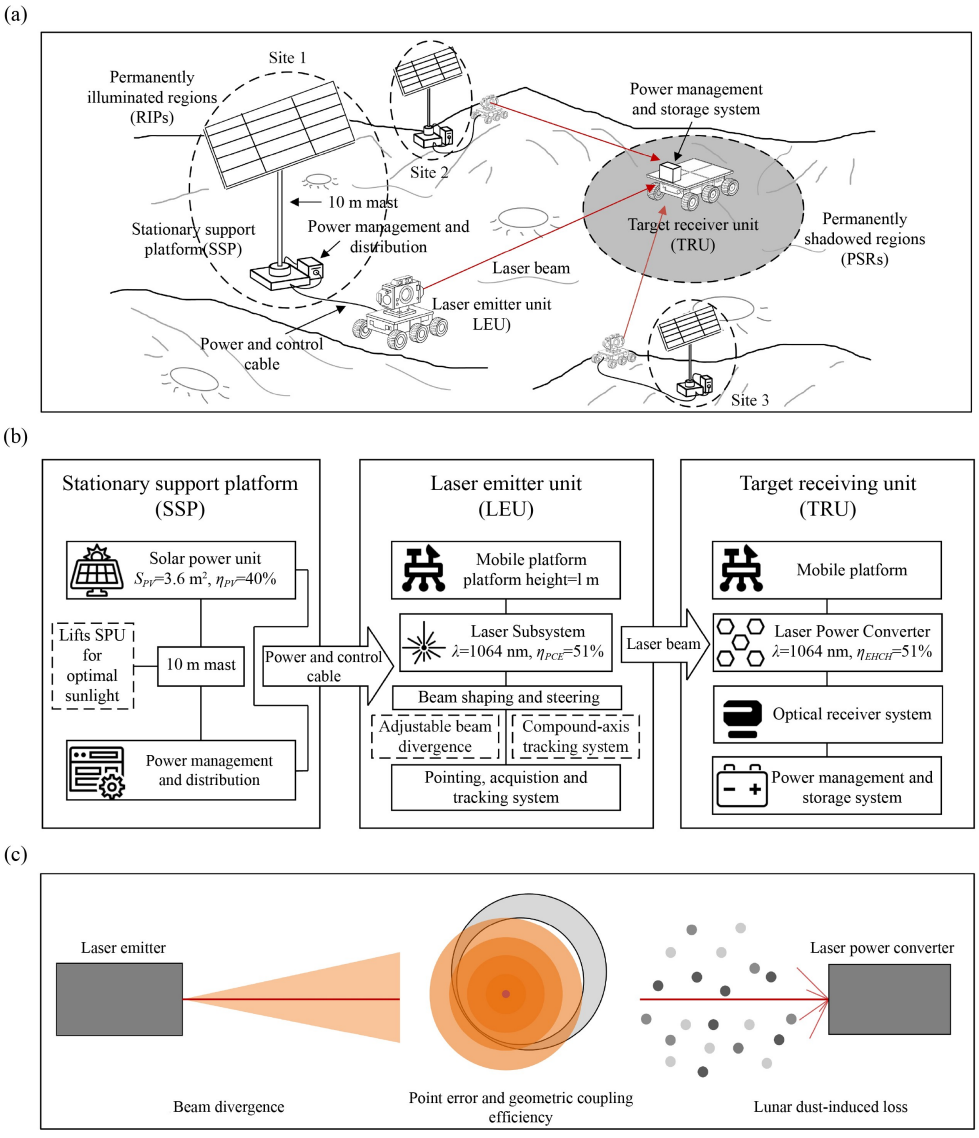

Fig. 1 Schematic of the lunar LWPT system. (a) Multi-site laser power transmission network system. (b) Energy flow and subsystems. (c) Key laser attenuation factors during transmission.

TRU—typically mounted on another mobile platform—employs an Optical Receiver System to capture the incoming laser beam. A Laser Power Converter (LPC) then efficiently transforms the optical energy back into electrical form, which is subsequently managed and stored by a Power Management and Storage System (PMSS). In our simulation framework, every valid grid point across the terrain surface is treated as a potential TRU location, enabling comprehensive evaluation of spatial coverage performance.

It should be emphasized that laser propagation across the lunar surface is subject to significant physical attenuation effects, as schematically illustrated in Fig. 1(c). Key loss mechanisms include: (i) beam divergence due to diffraction, (ii) pointing errors and geometric coupling inefficiencies arising from PAT system imperfections, and (iii) atmospheric attenuation induced by suspended lunar dust particles. The following subsection presents a rigorous mathematical formulation of these critical efficiency-degrading factors.

2.2 Laser power transmission model

To quantify the end-to-end power transfer efficiency from any LEU to a TRU, this study establishes a comprehensive link budget model that accounts for transmit power, beam divergence, pointing error, and lunar dust attenuation. The electrical power received at the TRU is expressed as (Donmez et al., 2023; Naqbi et al., 2024a)

$$P_h = P_t \cdot \eta_{\text{geom}} \cdot L_p \cdot L_{\text{dust}} \cdot \eta_{\text{EHCH}}, \quad (1)$$

where P_h is the received electrical power, P_t is the optical transmit power, η_{geom} is the geometric coupling efficiency determined by beam diffraction and finite receiver aperture size, L_p is the power loss factor induced by pointing errors at both transmitter and receiver, L_{dust} is the attenuation factor due to propagation through lunar dust, η_{EHCH} is the optoelectronic conversion efficiency at the receiver.

2.2.1 Transmit power

The available laser power is fundamentally constrained by local solar insolation at the deployment site. The transmit optical power P_t is modeled as

$$P_t = (P_S \cdot \eta_{\text{illum}} \cdot S_{PV} \cdot \eta_{PV}) \cdot \eta_{PCE}, \quad (2)$$

where P_S is the solar constant, η_{illum} is the site-specific annual average illumination ratio, S_{PV} is the photovoltaic array area, η_{PV} is the photovoltaic conversion efficiency, The term in parentheses represents the stable electrical input power that the SSP can supply to the LEU. This power is then converted into laser output via a laser subsystem with electro-optical conversion efficiency η_{PCE}, forming the transmitted beam.

2.2.2 Beam divergence and geometric coupling efficiency

In free space, laser beams diverge due to diffraction, causing energy density to decrease with propagation distance. To accurately capture this effect, we adopt a physical optics-based TEM_{00} Gaussian beam model rather than simplified geometric or far-field antenna gain approximations. The irradiance $I(r,z)$ on a plane perpendicular to the propagation axis is given by

$$I(r,z) = \frac{2P_t}{\pi w^2(z)} exp(-\frac{2r^2}{w^2(z)}), \quad (3)$$

where $w(z) = w_0\sqrt{1+\left(\frac{\lambda z}{\pi w_0^2}\right)^2}$ is the beam radius at propagation distance z, λ is the laser wavelength, and w_0 is the beam waist radius located at the transmitter aperture ($z = 0$). In this study, we assume the beam is collimated at the output, such that the beam waist coincides with the transmitter plane (Andrews and Phillips, 2005).

The geometric coupling efficiency η_{geom} is defined as the fraction of total beam power captured by a circular receiver aperture of radius $d_r/2$. Integrating the irradiance over the receiver area yields:

$$\eta_{\text{geom}} = 1 - \exp(-\frac{d_r^2}{2w(z)^2}). \quad (4)$$

This formulation precisely quantifies power loss due to beam spreading and finite aperture size.

2.2.3 Pointing loss factor

Pointing jitter or misalignment is a critical source of power loss in LWPT systems. Small angular deviations cause the beam centroid to shift away from the receiver center, significantly reducing collected power. It is implicitly assumed that the laser beam propagation is paraxial, which is a valid approximation for long-distance terrestrial and space-based laser links where the ratio of aperture size to distance is small (Andrews and Phillips, 2005). This model assumes that the pointing error follows a zero-mean Gaussian distribution, which is widely adopted in free-space optical links to represent random perturbations caused by platform vibrations, thermal drifts, and control system noise (Arnon, 2003; Farid and Hranilovic, 2006). The resulting power loss factor, denoted as L_p is expressed as the product of the transmitter-side loss L_t and the receiver-side loss L_r:

$$L_p = L_t \cdot L_r, \quad (5)$$

where

$$L_t = \exp(-G_t\phi_t^2), \quad (6)$$

$$L_r = \exp(-G_r\phi_r^2), \quad (7)$$

where ϕ_t and ϕ_r are the root-mean-square (RMS) radial pointing error angles at transmitter and receiver, respectively. The RMS values are composite and include contributions from both mechanical platform vibrations (jitter/sway) and static misalignment errors projected onto the receiver plane (Arnon, 2003). $G_t \approx (\pi d_t/\lambda)^2$ and $G_r \approx (\pi d_r/\lambda)^2$ are dimensionless parameters associated with the transmitter and receiver apertures. d_t and d_r are the transmitter and receiver aperture diameters. In this model, G_t and G_r do not function as conventional antenna gains in the link budget. Instead, they serve as sensitivity factors to pointing error: the larger the G value, the narrower the beam, and consequently, the greater the power loss induced by pointing misalignment.

2.2.4 Lunar dust attenuation

Attenuation of laser transmission caused by suspended lunar dust particles occurs primarily through two physical mechanisms: absorption and scattering. When a laser beam propagates through a medium containing such particles, the resulting power attenuation can be quantitatively modeled using a modified Beer-Lambert law (Bohren and Huffman, 2004). The attenuation factor,

denoted as L_{dust} is expressed as

$$L_{\text{dust}} = e^{-\int C_{\text{ext,avg}} \times N(h(l))\mathrm{d}l}, \tag{8}$$

where $C_{\text{ext,avg}}$ is the ensemble-averaged extinction cross-section of lunar dust particles, $N(h(l))$ denotes the number density of dust particles at altitude h above the lunar surface, evaluated at path point l.

The computation of the extinction cross-section C_{ext} must be based on a physically appropriate scattering model. The choice among Rayleigh scattering, Mie scattering, and geometric optics depends on the relative size of the particle radius r to the laser wavelength λ. In this study, the laser operates at $\lambda = 1064$ nm. Analyses of Apollo returned samples indicate that the particle size distribution (PSD) of lunar dust peaks in the range of 100−300 nm. Since the particle radius r (100−300 nm) is comparable to the laser wavelength λ (1064 nm), neither Rayleigh scattering($r \ll \lambda$) nor geometric optics($r \gg \lambda$) is applicable. Therefore, Mie Scattering theory—the most physically accurate approach for this size regime—is adopted in this work to compute C_{ext}.

For a single spherical particle of radius r, the extinction cross-section $C_{\text{ext}}(r)$ can be expressed as

$$C_{\text{ext}}(r) = \frac{2\pi}{k_{\text{wav}}^2} \sum_{n=1}^{n_{\max}} (2n+1) Re(a_n + b_n), \tag{9}$$

where $k_{\text{wav}} = \dfrac{2\pi}{\lambda}$ is the wave number of the laser in vacuum, a_n and b_n are the Mie scattering coefficients, defined as

$$\begin{cases} a_n = \dfrac{m\psi_n(mx)\psi'_n(x) - \psi_n(x)\psi'_n(mx)}{m\psi_n(mx)\varsigma'_n(x) - \varsigma_n(x)\psi'_n(mx)} \\ b_n = \dfrac{\psi_n(mx)\psi'_n(x) - m\psi_n(x)\psi'_n(mx)}{\psi_n(mx)\varsigma'_n(x) - m\varsigma_n(x)\psi'_n(mx)} \end{cases}, \tag{10}$$

where m is the complex refractive index of the lunar dust particles, and $x = \dfrac{2\pi r}{\lambda}$ is the dimensionless size parameter. The functions ψ_n and ς_n are the Riccati-Bessel functions, defined in terms of the spherical Bessel functions of the first kind (j_n) and the spherical Hankel functions of the first kind ($h_n^{(1)}$) as $\psi_n(\rho) = \rho j_n(\rho)$ and $\varsigma_n(\rho) = \rho h_n^{(1)}(\rho)$, where ρ denotes the argument. The primes denote derivatives with respect to the argument.

Lunar dust particles are not monodisperse but typically follow a size distribution. In this study, the probability density function of particle radius is modeled using a log-normal distribution $P(r)$:

$$P(r, \mu_{LN}, \sigma_{LN}) = \frac{1}{r\sigma_{LN}\sqrt{2\pi}} exp\left(-\frac{(\ln r - \mu_{LN})^2}{2\sigma_{LN}^2}\right), \tag{11}$$

where μ_{LN} and σ_{LN} are the mean and standard deviation of the natural logarithm of the particle radius, respectively.

Therefore, the ensemble-averaged extinction cross-section $C_{\text{ext,avg}}$ can be computed as

$$C_{\text{ext,avg}} = \frac{\int C_{\text{ext}}(r) P(r; \mu_{LN}, \sigma_{LN})\mathrm{d}r}{\int P(r; \mu_{LN}, \sigma_{LN})\mathrm{d}r}. \tag{12}$$

To accurately characterize the attenuation effect of suspended lunar dust on the laser link, a physically grounded dust density profile must be constructed based on observational data. In this study, we adopt a comprehensive hybrid dust model to precisely capture the vertical variation of particle number density within the lunar exospheric dust layer.

The model employs a power-law distribution to describe the dependence of dust number density N on altitude h above the lunar surface. This formulation effectively captures the suspension state of dust under the combined influence of the Moon's weak gravity and near-surface electrostatic fields. The mathematical expression is given by

$$N(h) = \begin{cases} N_{1,\text{near}} \cdot h^{-\alpha_{\text{near}}}, & \text{if } h \leqslant 30 \\ N_{1,\text{high}} \cdot h^{-\alpha_{\text{high}}}, & \text{if } h > 30 \end{cases}, \tag{13}$$

where α_{near} and α_{high} are the power-law exponents governing the vertical decay rates in the near-surface and high-altitude regimes, respectively. Specifically, for the near-surface regime ($h \leqslant 30$ m), dust suspension is primarily governed by surface photoelectric effects and the plasma sheath. Above 30 m, dust particles predominantly follow ballistic trajectories. The model parameters are calibrated to ensure continuity of N at the transition altitude, enabling a high-fidelity simulation of the vertical dust density profile.

3 Laser deployment position optimization based on multi-objective genetic algorithm

3.1 Problem formulation and objective functions

The decision variable X is a mixed-integer vector encompassing both site selection and fine-tuning of positional coordinates. Consequently, for a candidate pool comprising N_{SSP} selectable sites, the optimization problem possesses a variable space of dimensionality $N_{SSP} + 2N_{LEU}$ (in this study, each SSP is connected to exactly one LEU, hence $N_{SSP} = N_{LEU}$) with the following structure:

$$X = [s_1, \Delta x_1, \Delta y_1, s_2, \Delta x_2, \Delta y_2, \ldots, s_{N_{SSP}}, \Delta x_{N_{LEU}}, \Delta y_{N_{LEU}}], \tag{14}$$

where $s_i \in \{0,1\}$ is a binary variable indicating whether the i candidate site is selected, and $\{\Delta x_i, \Delta y_i\}$ is a continuous variable representing the positional offset of the LEU from its reference location (i.e., the SSP position) if site i is activated.

For any given decision vector X, the three-dimensional Cartesian coordinates $(x_i^{LEU}, y_i^{LEU}, z_i^{LEU})$ of the Laser Emitter Unit (LEU) at an activated candidate site $i$are determined as follows:

$$\begin{cases} \left(x_i^{LEU}, y_i^{LEU}\right) = \left(x_i^{SSP}, y_i^{SSP}\right) + (\Delta x_i, \Delta y_i) \\ z_i^{LEU} = Z_{\text{terrain}}\left(x_i^{LEU}, y_i^{LEU}\right) + h_{\text{vehicle}} \end{cases}, \tag{15}$$

where (x_i^{LPTS}, y_i^{LPTS}) denotes the horizontal reference coordinates of the LPTS site i (i.e., the SSP location), Z_{terrain} is the local terrain elevation interpolated from LOLA altimetry data, and h_{vehicle} is the fixed height of the LEU platform (e.g., a lunar rover) above the ground surface.

MOGA requires the definition of multiple performance objectives. We formulate the objective function vector F in terms of effective coverage ratio, regional connectivity ratio, and number of deployed LPTS units—representing system performance and deployment cost, respectively.

$$\begin{cases} F_1(X) = f_{\text{cost}}(X) \\ F_2(X) = f_{\text{coverage}}(X) \\ F_3(X) = f_{\text{connectivity}}(X) \end{cases}, \tag{16}$$

where $f_{\text{cost}}(X)$ denotes the deployment cost per LPTS unit (assumed constant), $f_{\text{coverage}}(X)$ is the ratio of effective coverage area to total feasible terrain area under deployment configuration X, and $f_{\text{connectivity}}(X)$ is the ratio of the largest connected component's area to the total effective coverage area—quantifying the network's topological connectivity.

3.1.1 Cost and complexity

In this study, the number of deployed LPTS is adopted as a key metric for mission cost and operational complexity, and is minimized as one of the independent objectives. The total number of active sites is determined by the binary selection variables s_i in the decision vector X, and can be expressed as

$$F_1(X) = \sum_{i=1}^{N_{SSP}} s_i. \tag{17}$$

where N_{SSP} is the total number of candidate sites in the deployment pool, and $s_i \in \{0,1\}$ is a binary variable defined as

$$s_i = \begin{cases} 1, & \text{if site } i \text{ is selected,} \\ 0, & \text{otherwise.} \end{cases}. \tag{18}$$

3.1.2 Effective coverage breadth of laser power transmission

In this study, the spatial extent of effective energy coverage provided by the LPTS network is quantified using the metric of effective coverage area.

For any grid cell j within the study region, the total received laser power $P_{\text{total},j}$ is computed by summing contributions from all activated LEUs, as governed by Eq.(1). The expression is given by

$$P_{\text{total},j}(X) = \sum_{i=1}^{N_S} P_h(i,j,X) \cdot I_{LoS}(i,j,X), \tag{19}$$

where N_s is the number of selected (activated) LPTS sites. $I_{LoS}(i,j,X)$ is an indicator variable representing the line-of-sight (LoS) visibility between LEU i and grid cell j:

$$I_{LoS}(i,j,X) = \begin{cases} 1, & \text{Unobstructed,} \\ 0, & \text{Obstructed.} \end{cases}. \tag{20}$$

Therefore, the effective coverage ratio $f_{\text{coverage}}(X)$—the fraction of the total study area that receives sufficient laser power—is defined as

$$f_{\text{coverage}}(X) = \frac{A_{\text{cell}} \cdot \sum_{j=1}^{N_{\text{grid}}} I\left(P_{\text{total},j}(X) \geqslant P_{\text{thresh}}\right)}{A_{\text{total}}}. \tag{21}$$

where A_{cell} denotes the area of grid cell, N_{grid} is the total number of grid cells within the study area, P_{thresh} is the minimum received power threshold required for operational functionality, A_{total} represents the total terrain area, $I(\cdot)$is the indicator function.

3.1.3 Regional connectivity metric

This study evaluates the spatial aggregation of effectively covered areas using a regional connectivity metric, which is computed based on connected component analysis in graph theory. Starting from the set of effectively covered points obtained in the previous section, a binary effective coverage map $M_{eff}(X)$ is generated, where grid cells that are effectively covered are assigned a value of 1, and all others are set to 0. Using 8-connected component analysis, all contiguous coverage regions $C_1, C_2, ..., C_k$ are identified. Among these, the Largest Connected Component (LCC) is determined by comparison. The connectivity ratio $f_{\text{connectivity}}(X)$ is then calculated as

follows:

$$f_{\text{connectivity}}(X) = \frac{\text{area}(LCC(M_{eff}(X)))}{\text{area}(M_{eff}(X))} = \frac{\max_k \text{area}(C_k)}{\sum_k \text{area}(C_k)}. \tag{22}$$

3.2 Multi-objective genetic optimization algorithm

To address the aforementioned complex optimization problem involving multiple conflicting objectives, this study employs MOGA. The algorithm utilizes the elitist Non-dominated Sorting Genetic Algorithm II (NSGA-II) as its core solver. NSGA-II has been extensively adopted in the field due to its superior performance in handling multi-objective optimization challenges and its robust capability in preserving solution diversity within the Pareto front.

3.2.1 Genetic algorithm

1. Mixed-integer vector individuals

In the NSGA-II framework, each individual (representing a deployment configuration) is encoded as a mixed-integer vector (chromosome), as illustrated in Fig. 2(a). This vector comprises two distinct segments.

1) Site Selection Genes: a binary vector of length N (where N is the total number of candidate sites), with each element $s_i \in \{0,1\}$ indicating whether site i is selected for deployment ($s_i = 1$) or not ($s_1 = 0$).

2) LEU Position Offset Genes: a continuous real-valued vector of length $2N$ where each pair of elements $(\Delta x, \Delta y)$ encodes the fine-grained positional offset of the LEU associated with site i relative to its reference SSP location in the easting and northing directions.

2. Pareto dominance

In multi-objective optimization, solution quality is evaluated relatively rather than absolutely, based on the principle of Pareto dominance. A solution $\boldsymbol{x}_A$ is said to dominate another vector $\boldsymbol{x}_B$ (denoted $\boldsymbol{x}_A \prec \boldsymbol{x}_B$), if it is no worse in all objectives and strictly better in at least one. Formally, for a minimization problem:

$$\begin{cases} \forall k \in \{1,2,..,M\}:\ f_k(\boldsymbol{x}_A) \leqslant f_k(\boldsymbol{x}_B) \\ \exists j \in \{1,2,..,M\}:\ f_j(\boldsymbol{x}_A) < f_j(\boldsymbol{x}_B) \end{cases}, \tag{23}$$

where M is the number of objective functions. Solutions not dominated by any other are termed non-dominated or Pareto-optimal, and their collective set constitutes the Pareto front.

3. Non-dominated sorting

NSGA-II employs a fast non-dominated sorting mechanism to hierarchically classify the population based on Pareto dominance relationships. All non-dominated solutions in the population are assigned to the first front (rank 1). These solutions are then temporarily removed from consideration, and the next set of non-dominated solutions among the remaining individuals is identified and assigned to the second front (rank 2). This process is iteratively repeated until every individual in the population is assigned a rank. The resulting hierarchy reflects the relative dominance level of each solution, forming a layered structure where lower ranks correspond to better performance across the objective space.

4. Crowding distance

To maintain diversity among solutions within the same Pareto front, NSGA-II introduces the Crowding Distance (CD) as a density estimator. For an individual 1 in a given rank, its crowding distance d_i is defined as the sum of normalized distances to its two nearest neighbors along each objective dimension:

$$d_i = \sum_{m=1}^{M} \frac{f_m(i+1) - f_m(i-1)}{f_m^{\max} - f_m^{\min}}, \tag{24}$$

where $f_m(i+1)$ and $f_m(i-1)$ are the values of the $m-th$ objective function for the two adjacent solutions when the population is sorted according to i, $f_m^{\max}$ and $f_m^{\min}$ denote the maximum and minimum values of objective m within the current front. It is important to note that to address the scale differences between objectives (as defined in Section 3.1), the standard NSGA-II procedure implicitly normalizes the objective values by the range of the current front during the crowding distance calculation (Deb et al., 2002). Solutions at the boundaries of the Pareto front are assigned infinite crowding distance to ensure their preservation during selection. This mechanism promotes a well-distributed approximation of the Pareto front by favoring less crowded regions in the objective space.

5. Individual selection

To construct the mating pool for generating the next generation, this study employs the classic binary tournament selection mechanism from NSGA-II, as illustrated in Fig. 2(b). In each tournament, two individuals are randomly selected from the current population (of size N). Their relative fitness is evaluated through a hierarchical comparison.

1) Rank Comparison: if the two individuals belong to different non-dominated fronts (i.e., have different ranks), the one with the lower rank—indicating superior dominance status—is selected as the winner.

2) Crowding distance comparison: if both individuals share the same rank, the one with the larger crowding distance is preferred. This promotes diversity by favoring solutions located in sparsely populated regions of the objective space.

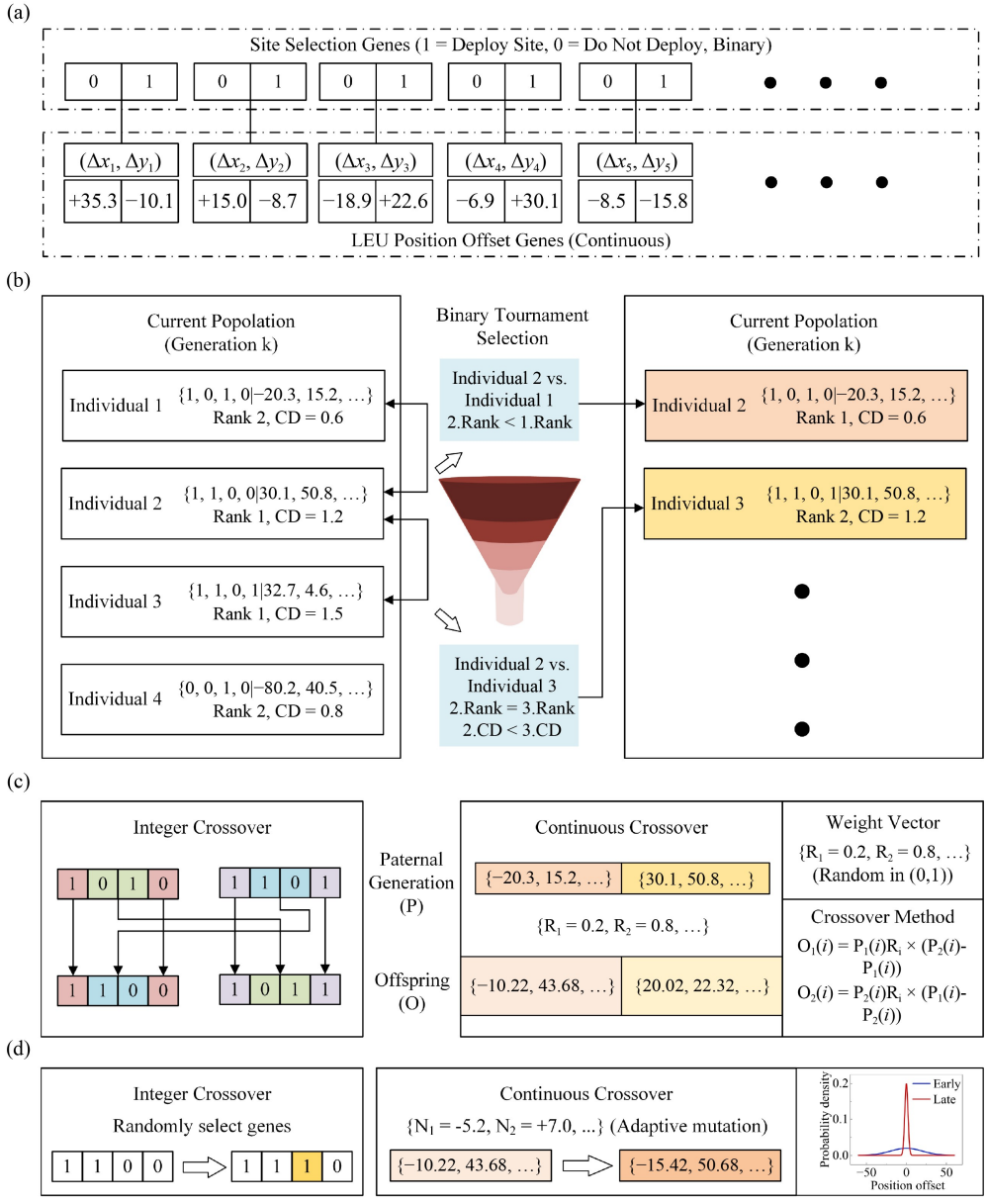

Fig. 2 Schematic of the NSGA-II-based optimization process. (a) Chromosome encoding with binary site selection genes and continuous position offset genes. (b) Binary tournament selection based on rank and crowding distance. (c) Crossover operation combining two-point recombination for binary segments and intermediate recombination for continuous segments. (d) Mutation operations including uniform bit-flip for binary genes and adaptive Gaussian perturbation for continuous genes.

3) The winning individual is placed into the mating pool. This process is repeated N times (with replacement), resulting in a mating pool of size N. The individuals in this pool are then used as parents for crossover and mutation operations in the subsequent evolutionary cycle.

6. Hybrid genetic operators

Genetic operations—crossover and mutation—are the primary drivers of population evolution in the proposed optimization framework. Given the hybrid nature of the decision variables (binary selection and continuous offset), distinct operators are applied to different segments of the chromosome.

1) Crossover Operation: crossover generates new offspring by recombining genetic information from two parent individuals, as illustrated in Fig. 2(c). For binary site selection genes: a two-point crossover is employed. Two crossover points are randomly selected on the binary segment of the chromosome, dividing it into three parts. The first offspring O_1 inherits the head and tail segments from parent P_1 and the middle segment from P_2, the second offspring O_2 receives the complementary structure. For continuous position offset genes: An

intermediate recombination (weighted averaging) operator is used. This method preserves the statistical properties of the parent solutions while generating new real-valued vectors within the hyper-rectangle defined by the parents. For parents P_1 and P_2, the two offspring are computed as

$$\begin{cases} O_1 = P_1 + R \otimes (P_2 - P_1) \\ O_2 = P_2 + R \otimes (P_1 - P_2) \end{cases}, \tag{25}$$

where R is a random weight vector with each element independently sampled from a uniform distribution over (0,1), $\otimes$ denotes element-wise multiplication.

2) Mutation Operation: mutation introduces small random perturbations to individual chromosomes to maintain genetic diversity and prevent premature convergence, as shown in Fig. 2(d). For binary genes: Uniform mutation is applied. With a low mutation probability p_m, one or more bits are randomly selected and flipped (0 to 1 or 1 to 0), enabling occasional activation or deactivation of candidate sites. For continuous genes: Adaptive feasible Gaussian mutation is adopted. For a continuous gene $c(i)$ in individual c, its mutated value $c'(i)$ is given by

$$c'(i) = c(i) + N(0, \sigma^2), \tag{26}$$

where $N(0, \sigma^2)$ denotes a random sample from a zero-mean Gaussian distribution with standard deviation σ. The parameter σ is adaptively adjusted during evolution: larger values are used in early generations to promote global exploration, while smaller values are adopted in later stages to enable fine-grained local search.

3.2.2 Multi-objective optimization

In this study, a fundamental trade-off exists among the objectives: while minimizing the number of deployed stations reduces mission cost and complexity, increasing their number enhances both effective coverage and regional connectivity. Deploying more LPTS enables illumination from diverse vantage points, thereby expanding the total covered area and bridging isolated coverage regions that would otherwise remain disconnected. Conversely, reducing station count inevitably leads to performance degradation in terms of coverage breadth and network robustness.

Therefore, the goal of the multi-objective genetic algorithm is not merely to minimize deployment scale, but to identify, for each feasible number of stations, the optimal combination and precise placement of LPTS units that maximizes coverage performance—defined as the joint metric of coverage ratio and connectivity. The algorithm ultimately generates a set of Pareto-optimal solutions, which explicitly quantifies the marginal performance gain (in coverage and connectivity) achieved per additional station. This provides mission planners with a scientifically grounded, data-driven decision support framework for balancing infrastructure investment against system performance.

The detailed optimization workflow is illustrated in Fig. 3(a).

1. **Initialization:** a population of N individuals is randomly generated. Each individual (chromosome) represents a candidate deployment solution encoded as a hybrid decision vector, with binary site selection genes and continuous position offset genes initialized within their predefined bounds.

2. **Fitness Evaluation:** for each individual X in the population, the following steps are performed—illustrated in Fig. 3(b).

1) Solution decoding: extract the activated sites b_i and the precise LEU coordinates from the chromosome.

2) Power transmission calculation: for every target grid point j, perform a LoS check with each selected LEU i. If unobstructed, compute the received power P_h^i using Eq.(1), as shown in Fig. 3(c).

3) Objective evaluation: compute the number of deployed stations $f_1(X) = \sum b_i$; Calculate the effective coverage ratio $f_2(X)$ by counting the fraction of grid cells where $P_{\text{total},j} \geqslant P_{th}$, according to Eq.(21); Determine the regional connectivity ratio $f_3(X)$ via 8-connected component analysis, computing the proportion of the largest connected cluster to the total covered area, as defined in Eq.(22).

3. **Non-Dominated Sorting:** the entire population is ranked into non-dominated fronts based on Pareto dominance. Solutions not dominated by any other are assigned the highest rank (rank 1).

4. **Diversity Preservation:** to prevent clustering on the Pareto front, the crowding distance is computed for each solution within its rank. During selection, individuals with lower ranks are preferred; among solutions of equal rank, those with larger crowding distances are favored, promoting uniform distribution in the objective space.

5. **Genetic Operations:** offspring are generated through as follow.

1) Crossover: a two-point crossover is applied to the binary segment (site selection), while an intermediate recombination operator is used for the continuous variables (position offsets).

2) Mutation: apply uniform mutation to the binary part and adaptive Gaussian mutation to the continuous variable part.

6. **Elitism and Iteration:** the parent population and offspring population are first combined, followed by non-dominated sorting and crowding distance calculation.

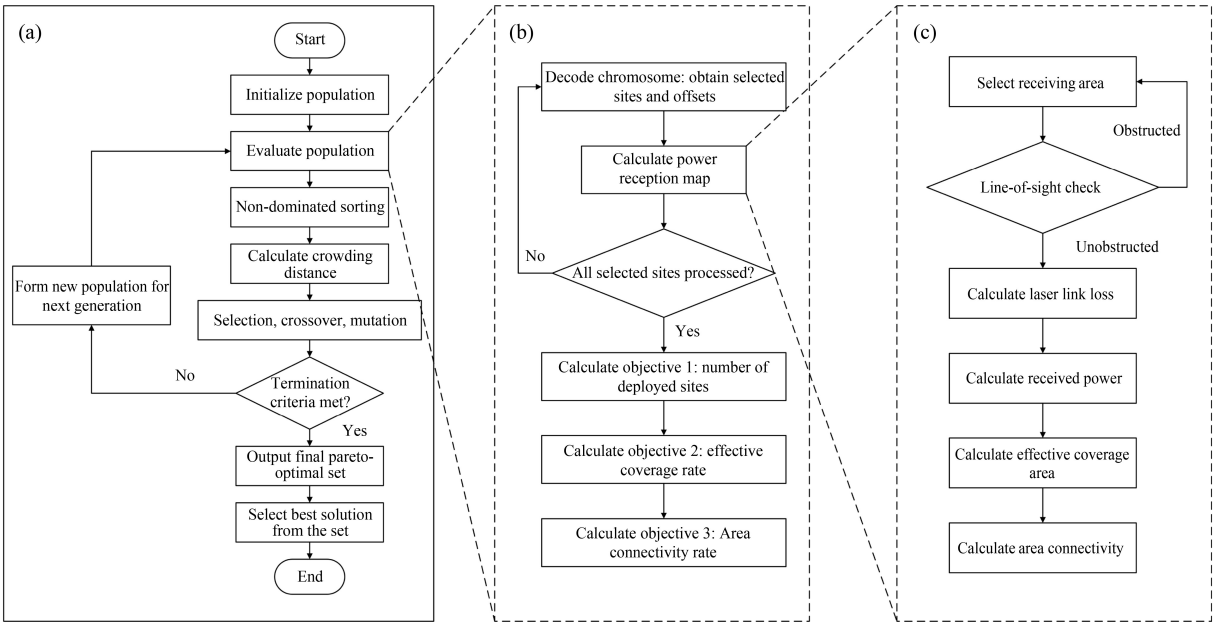

Fig. 3 Flowchart of the multi-objective optimization algorithm. (a) The main evolutionary loop of the NSGA-II processes. (b) Detailed subprocess for individual fitness evaluation. (c) Subprocess detailing the calculation of laser link loss and received power for each grid cell.

From this merged population, the best individuals are selected to form the next generation. This iterative process repeats until a predefined termination criterion is met.

The overall procedure aims to systematically explore the vast solution space and ultimately converge toward an approximate Pareto-optimal front, thereby providing decision-makers with a set of well-distributed, high-quality solutions that represent different trade-offs among the conflicting objectives.

4 Simulation results and analysis

4.1 Simulation setup

Shackleton Crater, renowned for its confirmed water ice deposits within PSRs and favorable illumination conditions at its rim, has been identified as a prime location for lunar south pole development, holding a significant position in the future lunar exploration plans of multiple nations and agencies (Creech et al., 2022; Wei et al., 2023). This region features three prominent high-illumination zones: SR1, SR2, and CR1 (Fig. 4(a)), all exhibiting annual average illumination rates exceeding 70%. Furthermore, some studies suggest that illumination rates at certain altitudes above these locations may even exceed 90% (Mazarico et al., 2011; Gläser et al., 2014; Wei et al., 2023). Therefore, based on the re-analysis of LOLA data by Barker et al. (2021), this study reconstructs the lunar surface topography near Shackleton Crater using cleaned and processed point cloud data from LOLA sites 1 and 4, establishing the terrain map for the study area (Fig. 4(b)). This dataset, processed with advanced orbit-crossover adjustments, eliminates orbital errors from the raw LOLA data, generating a high-resolution Digital Elevation Model (DEM) of up to 5 meters per pixel (5 m/pix). The rugged topography and prominent ridges near Shackleton Crater result in significant slope variations (Fig. 4(c)). This 5-meter resolution is a critical foundation for our optimization method, as it ensures that the proposed meter-level positional fine-tuning is physically meaningful for avoiding micro-terrain features (e.g., boulders, small ridge lines). On this DEM, a 10-meter horizontal adjustment can plausibly move an LEU from an obstructed LoS point to a visible one.

Within the Shackleton Crater vicinity covered by LOLA data, this study selected 9 candidate Stationary Support Platform (SSP) locations. These sites were chosen based on the annual average illumination rate data provided by Gläser et al. and are all situated in high-illumination zones (e.g., SR1, SR2, CR1). Each SSP is assumed to be equipped with a 10-meter mast to secure optimal illumination conditions, achieving an average illumination rate exceeding 85% (Mazarico et al., 2011; Gläser et al., 2014; Wei et al., 2023). The detailed coordinates and illumination rates of these candidate sites are presented in Table 1.

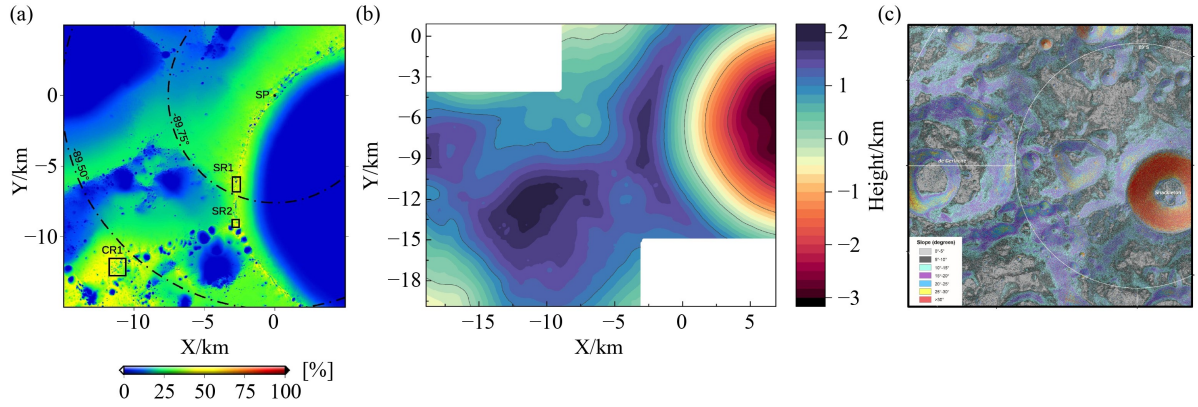

Fig. 4 Topography and illumination conditions of the Shackleton Crater study area. (a) Annual average illumination map, highlighting high-illumination zones SR1, SR2, and CR1 (Gläser et al., 2014). (b) Reconstructed DEM from LOLA data. (c) Slope map derived from the high-resolution DEM (Stopar and Meyer, 2019).

Table 1 Configuration of candidate LPTS sites

Region	Site ID	Coordinates (Lat, Lon)/(°)	Avg. Illumination/%
SR1	1	(−89.77, 203.46)	87.42
	2	(−89.78, 204.27)	87.41
	3	(−89.76, 202.69)	86.88
SR2	4	(−89.69, 197.05)	85.93
	5	(−89.69, 198.43)	85.19
	6	(−89.68, 196.63)	85.14
CR1	7	(−89.45, 222.69)	93.10
	8	(−89.43, 222.73)	92.53
	9	(−89.44, 223.28)	92.26

In this study, the effective power reception threshold for the TRU is set to 60W. This value is justified by referencing NASA's Volatiles Investigating Polar Exploration Rover (VIPER), where the combined power consumption of key instruments—such as the Neutron Spectrometer System (NSS, ~1.6W), Near-Infrared Volatiles Spectrometer System (NIRVSS, ~17W), and Mass Spectrometer (MSolo, ~35W)—is under 60W. Similarly, for the Curiosity rover, the combined power for instruments like the Chemistry and Mineralogy (CheMin) instrument, the Mars Hand Lens Imager (MAHLI), and the Alpha Particle X-ray Spectrometer (APXS) is also below 60W. Therefore, excluding thermal control and basic avionics, a 60W power threshold ensures that a stationary rover can simultaneously operate at least two critical scientific instruments for sustained observation and maintain core electronics. Even after accounting for these basic power draws, this threshold provides a net power budget of approximately 25W, sufficient to support a standard suite of scientific instruments (e.g., spectrometers, environmental sensors) for extended-duration continuous data acquisition.

Based on the models established above, the physical meanings and numerical values of the parameters used in this study are detailed in Table 2.

4.2 Analysis of simulation results

4.2.1 Analysis of the initial baseline scenario

To quantify the effectiveness of the MOGA method, an 'initial baseline scenario' is first defined. Referencing the study by Gläser et al. (2014), by selecting the three LPTS base sites with the highest average illumination rates. The coordinates are (−89.77, 203.46), (−89.69, 197.05) and (−89.45, 222.69), corresponding to Site IDs 1, 4, and 7 in Table 1. Their respective average illumination rates are 87.42%, 85.93%, and 93.10%. This baseline does not perform any positional fine-tuning or network topology optimization. Figure 5 illustrates the network coverage performance of this baseline scheme. Figure 5(a) shows the power reception map across the study area, and Fig. 5(b) provides a detailed coverage map with colored boundaries for areas covered by individual or combined stations. Within the total 441.34 km^2 of valid terrain, the baseline scenario achieves a total coverage area of 47.48 km^2, resulting in a coverage rate of 10.76% and a maximum regional connectivity of only 39.93%. This strongly demonstrates that a based solely on optimal local illumination fails in the complex terrain of the lunar polar region. Despite utilizing high-illumination sites, the coverage effectiveness is clearly deficient. The power supply zones formed by the individual stations are highly fragmented and 'island-like', lacking large-scale continuous coverage. The overall system robustness is low, making it unsuitable for lunar exploration missions that require continuous operations over wide areas.

Table 2 Simulation parameter setup

Parameter Category	Physical Quantity	Physical Meaning	Value
Environment	P_S	Solar constant	1353 W/m^2
	μ_{LN}	Log-mean of dust particle radius	1n (75 nm) (Park et al., 2008)
	σ_{LN}	Log-std. dev. of dust particle radius	1.6
	α_{high}	Dust power-law exponent (high-alt.)	2.7
	α_{near}	Dust power-law exponent (near-surface)	1.45
	m	Dust complex refractive index	1.58+0.01i
SSP	N_{SSP}	Number of candidate LPTS sites	9
	h_{mast}	LPTS mast height	10 m (Mazarico et al., 2011)
	η_{illum}	Avg. illumination at LPTS site	Table 1(Mazarico et al., 2011; Gläser et al., 2014; Wei et al., 2023)
	S_{PV}	SSP solar receiver area	3.6 m^2
	η_{PV}	Solar receiver efficiency	40%(Mukherjee et al. 2013, Ren et al., 2023)
LEU	h_{vehicle}	LEU platform height	1 m
	λ	Laser wavelength	1064 nm
	η_{PCE}	Electro-optical efficiency	51% (Lin et al., 2019)
	d_t	Emitter aperture diameter	0.1–5 mm (Fitness value)
	ϕ_t	Emitter pointing error angle	2.0 μrad (Grandidier et al., 2021)
TRU	η_{EHCH}	Power conversion efficiency	45%
	d_r	Receiver aperture diameter	2.1 m (Naqbi et al., 2024a)
	ϕ_r	Receiver radial error angle	0.1 μrad
	P_{thresh}	Power reception threshold	60 W
	T	Number of iterations	100
Optimize	N_0	Population size	100
	p_c	Crossover probability	0.8
	p_m	Mutation probability	Adaptive Gaussian distribution

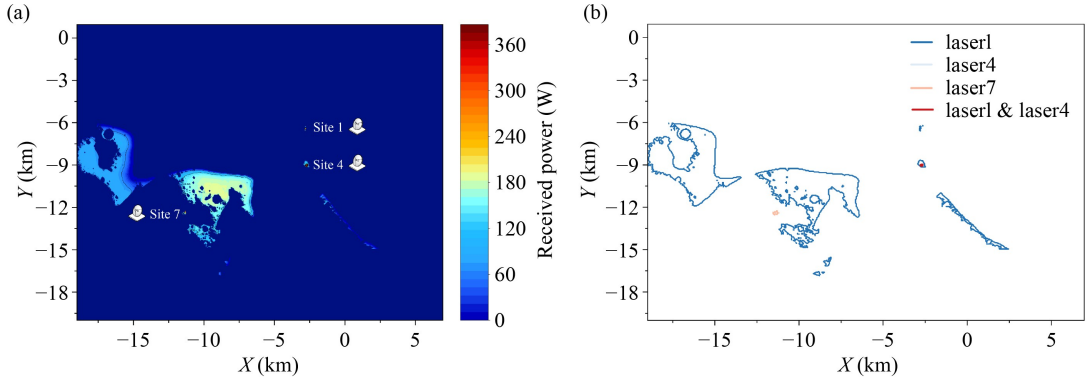

Fig. 5 Performance of the initial baseline deployment scenario. (a) Received power map (in Watts). (b) Detailed coverage boundaries for sites 1, 4, and 7.

4.2.2 Analysis of MOGA optimization results

To improve the effective coverage rate and regional connectivity, this study allows the LEUs to be repositioned within a 100-meter rectangular area around their initial sites, employing MOGA to find the optimal deployment locations. After 100 iterations, the MOGA algorithm converges to a Pareto-optimal front comprising multiple non-dominated solutions. Figure 6 displays the distribution of this final Pareto-optimal set in the objective space. Note that trivial solutions corresponding to zero deployed sites (zero cost, zero coverage) were

filtered from the final Pareto front analysis to focus on operationally viable configurations. The front intuitively reveals the quantitative trade-offs among the three objectives. As shown in Fig. 6(a), the effective coverage area generally expands as the number of stations increases. Notably, connectivity (Fig. 6(b)) exhibits a more complex relationship: as the number of sites increases from 3 to 4-5, the connectivity score paradoxically shows a clear decline. This reveals a non-intuitive conflict: in pursuit of higher total coverage, the algorithm may activate new, isolated coverage 'islands' far from the core network, thereby reducing the overall regional connectivity. This fully demonstrates the profound conflict between the objectives.

To select a single, well-balanced solution from the generated Pareto front for detailed analysis, this study employs the Technique for Order of Preference by Similarity to Ideal Solution (TOPSIS), a robust multi-criteria decision-making (MCDM) method. TOPSIS ranks the solutions by identifying the solution that is geometrically closest to the Positive Ideal Solution (PIS, the hypothetical best solution) and farthest from the Negative Ideal Solution (NIS, the hypothetical worst solution). Based on the mission priorities, the weights (W) for the three objectives were defined as: Coverage (W=40%), Connectivity (W=40%), and Number of Sites (W=20%). Furthermore, Coverage and Connectivity were defined as benefit-type criteria (higher is better), while Number of Sites was defined as a cost-type criterion (lower is better). The solution with the highest 'relative closeness' score was then identified as the 'Preferred Solution'. The selection is based on the relative closeness coefficient C_i for each solution i,which is calculated as

$$C_i = \frac{S_i^-}{S_i^+ + S_i^-}, \tag{27}$$

where S_i^+ is the Euclidean distance from solution i to the PIS, and S_i^- is the Euclidean distance from solution i to the NIS. The solution with the maximum C_i (closer to 1) was identified as the Preferred Solution.

For a detailed comparison, a representative 'Preferred Solution' is selected from the Pareto front, representing a well-balanced compromise between cost and performance (Fig. 6(c)). This solution not only identifies the optimal 3-site combination but also provides the optimal meter-level offset for each LEU. The optimization algorithm selected sites 3, 5, and 6, with the following optimal position offsets: (dx_3, dy_3) = (−61.18 m, −55.87 m), (dx_5, dy_5) = (−55.72 m, −48.69 m), (dx_6, dy_6) = (60.45 m, 85.49 m).

The final network performance of the LPTS deployment at the optimized locations is shown in Fig. 7. Compared to the initial state in Fig. 5, the performance improvement is substantial. As seen in Fig. 7(a), the previously fragmented coverage 'islands' have been successfully connected, forming a broad and highly contiguous core power network. The total effective coverage rate increased significantly from 10.76% to 27.55% (>156% improvement), and the maximum regional connectivity surged from 39.93% to 98.92%, achieving almost complete connectivity for the effectively covered area. This is further corroborated by the detailed site coverage map in Fig. 7(b). The area covered by two or more laser stations is significantly expanded and interconnected, granting the system enhanced fault tolerance and stability within the core operational zone. Even if one station temporarily fails, a detector can still receive power from other stations, thus ensuring mission continuity.

In summary, the MOGA-based deployment optimization design method for lunar laser stations proposed in this paper can effectively expand the network coverage area while simultaneously improving regional connectivity. Through simulation analysis based on lunar surface exploration data and a laser energy transmission model, the effectiveness and engineering application potential of this design method have been validated, providing a reliable solution for lunar surface exploration

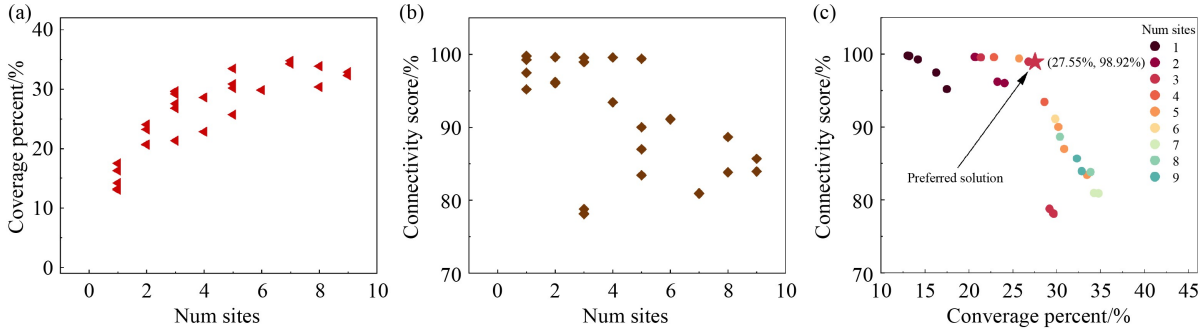

Fig. 6 MOGA Pareto-optimal solution set. (a) Coverage percent vs. number of sites. (b) Connectivity score vs. number of sites, showing a non-linear relationship. (c) The final Pareto-optimal front plotting connectivity vs. coverage, color-coded by the number of sites, and highlighting the selected 'Preferred Solution'.

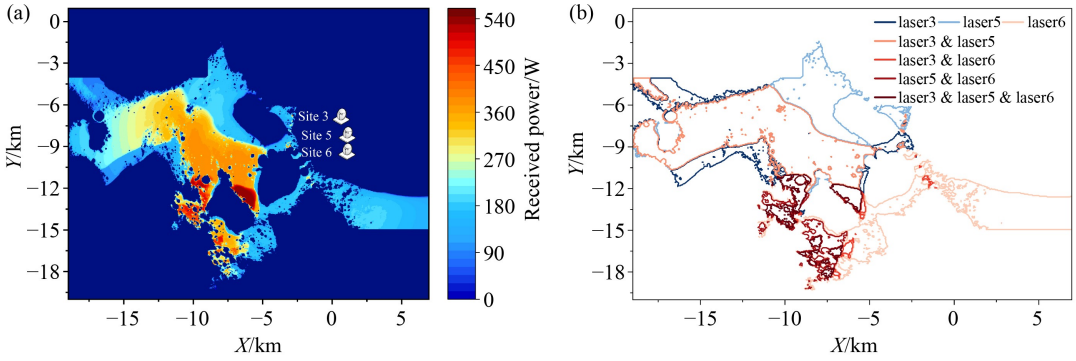

Fig. 7 Performance of the MOGA-optimized deployment scenario (Preferred Solution). (a) Received power map (in Watts). (b) Detailed coverage boundaries for sites 3, 5, and 6.

and infrastructure development.

5 Conclusions

This paper has successfully developed and validated an innovative optimization framework based on a Multi-Objective Genetic Algorithm (MOGA) to address the challenges of deploying a laser wireless power transmission network in the complex terrain and environment of the lunar south pole. The framework models the deployment as a mixed-integer optimization problem, seeking the optimal trade-off among three conflicting objectives: mission effectiveness (effective coverage), operational robustness (regional connectivity), and deployment cost (number of sites), using the NSGA-II algorithm as the solver. This study utilized 5-meter high-resolution topographic data from NASA's LOLA and integrated an advanced laser transmission model that accounts for lunar dust scattering effects, conducting a high-fidelity simulation analysis for LPTS deployment in the Shackleton Crater region.

Simulation results demonstrate that the baseline scenario, which relies solely on local illumination conditions, results in a highly fragmented power network with a total effective coverage of only 10.76% and poor regional connectivity (39.93%). This is insufficient to meet the demands of future lunar missions requiring large-scale, continuous operations. In contrast, the proposed MOGA method efficiently explores the complex solution space. Through a combined optimization of macro-scale site selection and micro-scale meter-level positioning, it successfully increased the effective coverage to 27.55% (a gain of over 156%) and elevated the maximum regional connectivity to 98.92%, establishing a continuous and stable laser power network. Furthermore, this research reveals the high sensitivity of the laser power system's performance to the precise deployment location of the emitter, emphasizing that optimizing for system-wide performance using high-resolution DEMs is critical to maximizing mission effectiveness.

The system model and optimization method established in this paper provide effective theoretical reference and technical support for the deployment of lunar laser power systems. However, some limitations persist. Primarily, the current model utilizes annual average illumination rates and fails to capture the complex, dynamic changes in light and shadow on the lunar surface over time. The model also focuses on the attenuation effects of suspended lunar dust on the laser beam, without yet incorporating the performance degradation caused by long-term dust accumulation and sedimentation on optical and photovoltaic surfaces. Future work will concentrate on introducing time-variant illumination models, considering more complex scenarios such as multi-rover cooperative power supply, and ultimately developing high-fidelity physical simulation testbeds to provide key technical support for autonomous lunar laser power systems.

Data availability

The data will be made available on request.

Acknowledgements

This work was financially supported in part by the National Natural Science Foundation of China (Grant Nos. 52575272, 52275241), the Fund for National Key Laboratory of Space Environment and Matter Behaviors (No. 2023059), the National Key Laboratory of Laser Spatial Information Foundation (No. LSI2025ZZKY02), and the National Key R&D Program of China (No. 2025YFF0511402).

Declaration of competing interest

Authors declare that they have no competing interests.

References

Abdollahzadeh S, Navimipour N J (2016). Deployment strategies in the wireless sensor network: a comprehensive review. Comput Commun, 91–92: 1–16

Andrews LC, Phillips RL(2005). Laser Beam Propagation through Random Media. SPIE: USA WA

Arnon S (2003). Effects of atmospheric turbulence and building sway on optical wireless-communication systems. Opt Lett, 28(2): 129–131

Barker M K, Mazarico E, Neumann G A, Smith D E, Zuber M T, Head J W (2021). Improved LOLA elevation maps for south pole landing sites: Error estimates and their impact on illumination conditions. Planet Space Sci, 203: 105119

Bohren CF, Huffman DR (2004). Absorption and scattering of light by small particles. New York: Wiley-CH Verlag GmbH & Co KGaA

Colaprete A, Schultz P, Heldmann J, Wooden D, Shirley M, Ennico K, Hermalyn B, Marshall W, Ricco A, Elphic R C, Goldstein D, Summy D, Bart G D, Asphaug E, Korycansky D, Landis D, Sollitt L (2010). Detection of water in the LCROSS Ejecta Plume. Science, 330(6003): 463–468

Creech S, Guidi J, Elburn D (2022). Artemis: an overview of NASA's activities to return humans to the Moon. In: 2022 IEEE Aerospace Conference (AERO). USA: IEEE

Deb K, Pratap A, Agarwal S, Meyarivan T (2002). A fast and elitist multiobjective genetic algorithm: NSGA-II. IEEE Trans Evol Comput, 6(2): 182–197

Shi D, Zhang L, Ma H, Wang Z, Wang Y, Cui Z (2016). Research on wireless power transmission system between satellites. In: 2016 IEEE Wireless Power Transfer Conference (WPTC). Portugal: IEEE

Donmez B, Azam I, Kurt G K (2023). Mitigation of misalignment errors over inter-satellite FSO energy harvesting : (Invited Paper). In: 2023 IEEE 34th Annual International Symposium on Personal, Indoor and Mobile Radio Communications (PIMRC). Toronto: IEEE

Farid A, Hranilovic S (2006). Outage probability for free-space optical systems over slow fading channels with pointing errors. In: 2006 IEEE LEOS Annual Meeting Conference Proceedings. Montreal: IEEE, 82–83.

Gläser P, Scholten F, De Rosa D, Marco Figuera R, Oberst J, Mazarico E, Neumann G A, Robinson M S (2014). Illumination conditions at the lunar south pole using high resolution Digital Terrain Models from LOLA. Icarus, 243: 78–90

Grandidier J, Jaffe P, Roberts W T, Wright M W, Fraeman A A, Raymond C A, Austin A, Lubin P, Sunada E T, Jones J P, Barchowsky A, Baker J D (2021). Laser power beaming for lunar night and permanently shadowed regions. Bullet AAS, 53(4)

He T, Yang S H, Zhang H Y, Zhao C M, Zhang Y C, Xu P, Muñoz M Á (2014). High-power high-efficiency laser power transmission at 100 m using optimized Multi-Cell GaAs Converter. Chin Phys Lett, 31(10): 104203

Höhn O, Walker A W, Bett A W, Helmers H (2016). Optimal laser wavelength for efficient laser power converter operation over temperature. Appl Phys Lett, 108(24): 241104

Landis G A (2020). Laser power beaming for lunar polar exploration. In: AIAA Propulsion and Energy 2020 Forum. American Institute of Aeronautics and Astronautics

Lin, H.-Y., Wu, M.-Y., Tang, J., Zhao, M.-J., and Sun, D., 2019. Compact Nd:YVO4 laser 1087.5 nm pumped by an edge-emitting LD. Optik, 185, 414–417

Mazarico E, Neumann G A, Smith D E, Zuber M T, Torrence M H (2011). Illumination conditions of the lunar polar regions using LOLA topography. Icarus, 211(2): 1066–1081

Mukherjee J, Jarvis S, Perren M, Sweeney S J (2013). Efficiency limits of laser power converters for optical power transfer applications. J Phys D Appl Phys, 46(26): 264006

Naqbi M, Loranger S, Kurt G K 2024a. Impact of lunar dust on Free Space Optical (FSO) energy harvesting. In: 2024 IEEE Aerospace Conference

Naqbi M, Loranger S, Kurt GK, (2024b). Optical power beaming in the lunar environment

Nozette S, Spudis P D, Robinson M S, Bussey D B J, Lichtenberg C, Bonner R (2001). Integration of lunar polar remote-sensing data sets: Evidence for ice at the lunar south pole. J Geophys Res, 106(E10): 23253–23266

Paige D A, Siegler M A, Zhang J A, Hayne P O, Foote E J, Bennett K A, Vasavada A R, Greenhagen B T, Schofield J T, McCleese D J, Foote M C, DeJong E, Bills B G, Hartford W, Murray B C, Allen C C, Snook K, Soderblom L A, Calcutt S, Taylor F W, Bowles N E, Bandfield J L, Elphic R, Ghent R, Glotch T D, Wyatt M B, Lucey P G (2010). Diviner lunar radiometer observations of cold traps in the Moon's South Polar region. Science, 330(6003): 479–482

Park, J., Liu, Y., Kihm, K.D., and Taylor, L.A., 2008. Characterization of Lunar Dust for Toxicological Studies. I: Particle Size Distribution. Journal of Aerospace Engineering, 21 (4), 266–271

Priyadarshi R, Gupta B (2021). Area coverage optimization in three-dimensional wireless sensor network. Wirel Pers Commun, 117(2): 843–865

Schorghofer N (2022). Gradual sequestration of water at lunar polar conditions due to temperature cycles. Astrophys J Lett, 927(2): L34

Ren, X.-N., Ge, C.-C., Chen, Z.-P., Irfan, Tu, Y., Zhang, Y.-C., Wang, L., Liu, Z.-L., and Guan, Y.-Q., 2023. Energy conversion materials for the space solar power station. Chinese Physics B, 32 (7), 078802

Siegler M, Paige D, Williams J P, Bills B (2015). Evolution of lunar polar ice stability. Icarus, 255: 78–87

Stopar J, Meyer H M (2019). Topographic Slopes (5-meter) of the Moon's South Polar Ridge

Wei G, Li X, Zhang W, Tian Y, Jiang S, Wang C, Ma J (2023). Illumination conditions near the Moon's south pole: Implication for a concept design of China's Chang'E−7 lunar polar exploration.

Acta Astronaut, 208: 74–81

Xu H, Du B, Shi D, Huang X, Hou X (2024a). Laser wireless power transfer system design for lunar rover. Space Solar Power and Wireless Transmission, 1(2): 129–135

Xu Z, Yang Z, Zheng G, Wan L, Wu Q, Dong Y, Lv Z, He T (2024b). Laser wireless power transmission based on spherical reflector intra-cavity beam splitting. Appl Opt, 63(22): 5840–5846

You W, Dong C, Cheng X, Zhu X, Wu Q, Chen G (2021b). Joint optimization of area coverage and mobile-edge computing with clustering for FANETs. IEEE Internet Things J, 8(2): 695–707

Zhang Y, Li Y, Zhang J (2024). Review of energy supply techniques for ice *in-situ* thermal mining in lunar permanently shadowed regions. Adv Space Res, 74(2): 784–799

Zheng Y, Zhang G, Huan Z, Zhang Y, Yuan G, Li Q, Ding G, Lv Z, Ni W, Shao Y, Liu X, Zu J (2024). Wireless laser power transmission: Recent progress and future challenges. Space Solar Power and Wireless Transmission, 1(1): 17–26

Zhong Z, Yashar M (2023). Lunar Economic Village Initiative (LEVI). In: ASCEND 2023. Las Vegas: American Institute of Aeronautics and Astronautics.

Zhou W, Jin K (2015). Efficiency evaluation of laser diode in different driving modes for wireless power transmission. IEEE Trans Power Electron, 30(11): 6237–6244

Zhou W, Jin K, Wang M, Wu Q (2020). Efficiency evaluation of laser based wireless power transmission system. In: 2020 IEEE Applied Power Electronics Conference and Exposition (APEC)

Zuniga A F, Turner M F, Rasky D, Loucks M, Carrico J, Policastri L (2017). Building an Economical and Sustainable Lunar Infrastructure to Enable Lunar Industrialization. In: AIAA SPACE and Astronautics Forum and Exposition. Orlando: American Institute of Aeronautics and Astronautics.